Use of drones to monitor water availability and quality in irrigation canals and reservoirs for improving water productivity and enhancing precision agriculture in smallholder farms

Tafadzwanashe Mabhaudhi[1], Tsitsi Bangira[2],
Mbulisi Sibanda[3], and Olufunke Cofie[1]

[1]International Water Management Institute, South Africa and Ghana
[2]Centre for Transformative Agricultural and Food Systems, University of KwaZulu-Natal, South Africa.

Abstract
The report provides a **methodology protocol** for measuring temporal and spatial changes in water quantity and quality using drone imagery. The procedure is informed by the need for effective and sustainable water resource use to enhance water productivity under climate change. It is based on a literature review that allows the identification of appropriate processes, materials, and procedures for water monitoring, including mapping spatial and temporal dynamics of reservoirs, measurement of water quality parameters, and flood mapping of irrigation canals.

Acknowledgement: We would like to thank all the funders who support this research through their contributions to the CGIAR Trust Fund. To learn more about TAFS-WCA and other initiatives in the CGIAR research portfolio, please visit https://www.cgiar.org/research/cgiar-portfolio/.

Suggested citation: Mabhaudhi, T.; Bangira, T.; Sibanda, M.; Cofie, O. 2022. *Use of drones to monitor water availability and quality in irrigation canals and reservoirs for improving water productivity and enhancing precision agriculture in smallholder farms.* Colombo, Sri Lanka: International Water Management Institute (IWMI). CGIAR Initiative on West and Central African Food Systems Transformation. 36p.

TABLE OF CONTENTS

LIST OF TABLES

LIST OF FIGURES

1 INTRODUCTION

Growing populations in developing countries rely on freshwater stored in small waterbodies for agricultural, domestic, mining and industrial use (Bangira et al., 2019; Sibanda et al., 2021). These water resources, especially those in Africa, are highly susceptible to climate variations and pollution and are generally insufficient to withstand these perturbations. Climate change is likely to affect the water cycle processes (e.g. precipitation, evaporation, runoff etc.) and water demand. Warmer temperatures increase the rate of evaporation of water into the atmosphere, in effect increasing the atmosphere's capacity to "hold" water. Increased evaporation may dry out some areas and fall as excess precipitation in other areas (Kundzewicz et al., 2018). Heavy downpours can increase the runoff into rivers and lakes, washing sediment, nutrients, pollutants, trash, animal waste, and other materials into water supplies, making them unusable, unsafe, or in need of water treatment (Tebbs et al., 2020).

Furthermore, the increasing impacts of anthropogenic activities on water resources negatively affect the quality and quantity of water stored in reservoirs. The impacts of climate change on water availability and quality will affect many sectors, including energy production, infrastructure, human health, agriculture, and ecosystems. Hence, there is a growing need to develop integrated, cheap and robust water quality monitoring approaches as a yardstick for achieving food and water security under climate change (Bangira et al., 2019). The use of unmanned aerial vehicles (UAVs) at catchment or waterbody scale allows accessing real-time information on the water resource and monitoring quality and quantity at different seasons. The specific objectives of the report are:

i. to provide a detailed methodology for assessing the feasibility of using drones in detecting and mapping flooding or leaks along irrigation canals and dams, and

ii. to provide a detailed methodology for assessing the spatial and temporal resolution capabilities of drones in detecting and mapping the levels and quality of water in irrigation canals and dams.

2 BACKGROUND AND LITERATURE REVIEW

This report builds on a systematic review of the available models for remotely sensed drone technologies in surface water resources monitoring and assessment (Sibanda et al., 2021). The review provided an in-depth systematic assessment of the literature on progress, challenges,

and opportunities in utilising UAVs in mapping and monitoring surface water resources for improving food production in smallholder farms in the global south. It highlighted the available bands and spatial and spectral resolutions of sensors appropriate for monitoring water resources to promote food and water security. Most importantly, the review listed the available models that have been applied in monitoring surface water quality and quantity using remotely sensed images acquired by drones. It is worth noting that the review also found that the most widely used sections of the electromagnetic spectrum in detecting specific water quality parameters were the visible section (blue and green) and the NIR wavebands. Finally, the review evaluated progress, gaps, and challenges faced by the global south in utilising drone technologies for mapping and monitoring the quality and quantity of surface water bodies.

Several inversion algorithms based on empirical, semi-empirical, analytical and semi-analytical methods were identified in the review for estimating water quality parameters using drone imagery (Kapalanga et al., 2021; Kibena et al., 2014; Sibanda et al., 2021). Empirical algorithms, which are the most popularly used, are based on a statistical relationship, that is, regression (parametric and non-parametric) analysis, between the spectral (reflectance or radiance) data properties of optimal bands and measured water quality parameters (e.g., Chl-a, total suspended solids (TSS), chemical oxygen demand (COD), biological oxygen demand (BOD), Secchi disk depth (ZSD), temperature, nutrients etc.) (Gholizadeh et al., 2016; Gitelson, 1992). Generally, the information about the spectral characteristics of the measured water quality parameter is used to assist in the selection of suitable wavelength(s) or best model in the empirical approach. On the other side, the analytical models use bio-optical and radiation transmission models to simulate the dispersion of light in the atmosphere and water bodies to describe the relationship between water quality components and the radiance or reflection spectrum of off-water radiation (Gholizadeh et al., 2016). The semi-analytical and semi-empirical models combine the empirical and the analytical models. The accuracy of these models varies, depending on the spectral characteristics of bands used, atmospheric correction algorithms applied, spatial resolution and concentration of parameters (Tebbs et al., 2020). Generally, the models use the earth's surface's visible, red, and infrared bands to estimate water quality parameters.

The review's findings underscored the use of bio-optical analytical algorithms in water quality monitoring (Sibanda et al., 2021). The composition of the water body and radiation transmission procedure is rather complex since many factors need to be measured for the model

to be established, such as the inherent optical characteristics of water, adjacent characteristics, and water quality variables (Salama et al., 2012). In addition, the spectral resolution of most satellite sensors and those measured near the ground are inconsistent, which leads to some difficulties in model research. However, the review has positively pointed towards using empirical algorithms, which are simple and easy to operate. It can be refined by selecting more precise spectral channels to increase the accuracy of water quality parameters retrieval (Kapalanga et al., 2021).

3 PROPOSED METHODOLOGY

3.1 Data collection

3.1.1 Water quality parameters for irrigation

Water quality is a general descriptor of water's physical, chemical, thermal, and/or biological characteristics (Modiegi et al., 2020; Ritchie et al., 2003). Defining a single water quality parameter to meet all uses and user needs is difficult. The quality of irrigation water that is generally considered acceptable should be clear, odourless, and foamless with minimum turbidity (TDS < 1000 mg L^{-1}) and a specific conductance below 1.5 mmhos/m (Ritchie et al., 2003). Water quality needs to be frequently monitored if high-quality crops and yields are to be attained. For example, chemical oxygen demand (COD) and biochemical oxygen demand (BOD) are appropriate indicators for organic matter concentrations in irrigation water. When COD and BOD are high in irrigation water, much oxygen will be consumed during the decomposition of organic matter resulting in an anaerobic condition (Kim et al., 2020). In this process, soil oxides such as Fe3+, Mn5+ and SO42− will exhaust oxygen to reduce the oxidation-reduction potential. Subsequently, the generated iron, manganese, sulphides, and organic acids may limit crop uptake and the absorption of nutrients. This frequently results in stunted growth, poor quality, and reduced harvests. Water salinity is a major problem in irrigation waters (Zaman et al., 2018). Excess salt increases the osmotic pressure of the soil solution, a situation that can result in a physiological drought condition. The presence of excess sodium will result in a deterioration of the soil structure, thereby reducing water penetration into and through the soil.

The presence of aquatic vegetation and algae (**Error! Reference source not found.**) in i rrigation canals can result in substantial operational problems with economic implications in water supply systems and waste significant volumes of water. Reduction of hydrological capacity and flow speed in affected canals, water log lond-weirs, block irrigation systems and filters are some of the problems.

Figure 1: Growth of aquatic vegetation and algae in the irrigation canal

The presence of bacteria in irrigation water can potentially spread serious human infections, such as severe hemorrhagic and gastrointestinal diseases, through agricultural produce (Zaman et al., 2018). Among various microbial parameters, Chl-a and blue-green algae concentration are the strongest proxies used to assess water quality. Quantifying chlorophyll-a's concentration is a standard method of monitoring the microbial conditions of a water body (Kim et al., 2020).

Deriving water quality variables from remote sensing observations requires two main steps: (i) atmospheric correction to retrieve the water leaving signal and (ii) deriving water quality variables from the water leaving signal. Eventually, both steps could be combined and simultaneously carried out. Water quality variables that can be derived from optical observations are those with the property of changing the visible sunlight through absorption and/or scattering (Kirk, 1994), namely phytoplankton pigment (blue-green bacteria, Chl-a), suspended particulate matter (SPM), clarity and coloured dissolved organic matter. This study will focus on SPM, blue-green bacteria, clarity and Chl-a concentrations.

i. Representative in situ measurements

A boat will be used to navigate the water bodies for sample collection. In situ measurements of water quality parameters, specifically, Chl-a, will be collected during the summer (October – March) seasonal conditions. In particular, harmful algae usually bloom during the warm summer or when water temperatures are warmer than usual, and the water is calm (Kim et al., 2020). Sampling sites will be selected randomly to span the entire surface of the reservoir. The

sample size will be determined as a sufficient representation of the whole system, including deep and shallow areas, coves and main basins. Presampling of the dam will be conducted in Google Earth Pro, where the experimental reservoir's polygon is digitized. The digitized polygon will then be imported into ArcGIS 10.8, which will be used to generate sampling points. These points will then be uploaded into a hand-held Trimble Global Positioning System (GPS) with an accuracy of less than 100 cm. These locations will be used to navigate to each sample point for field data collection. In the field, the boat will be used to navigate to the sampling points.

The parameters measured in the field campaigns, the type of measurement and the method/equipment used are presented in **Error! Reference source not found.**.

Table 1: Parameters measured in field campaigns

Parameter	Type	Method/Equipment
Sky-sun downwelling irradiance - E_d	In-situ radiometer	Hyperspectral radiometer – TriOS RAMSES-ACC-VIS
Water leaving upwelling radiance - L_w	In-situ radiometer	Hyperspectral radiometer – TriOS RAMSES-ARC
Chlorophyll-a	Laboratory Analysis	Spectrophotometry
CDOM	In-situ	Fluorometer – TriOS microFlu
TSS	Laboratory Analysis	Total Suspended Solids Dried from 103 to 105°C
Seschi depth	Secchi Disk	Secchi disk, 20 or 30 cm in diameter used to measure water transparency or turbidity.

Error! Reference source not found. shows the layout presentation for CDOM measurements u sing a fluorometer. At each sampling point, the downwelling irradiance (Ed) and water-leaving upwelling radiance $\boldsymbol{L_w}$ signals will be recorded simultaneously at least three consecutive times together with the CDOM measurement. The recordings are calibrated automatically in the software of the equipment (MSDA_XE) using the calibration files provided by the manufacturer.

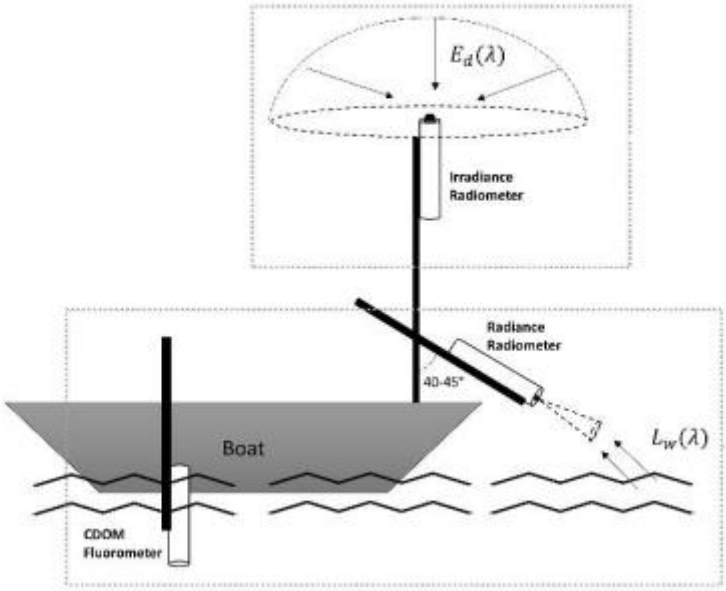

Figure 2: Layout configuration for radiometric and fluorometer measurements

For Chl-a, water samples will be collected in polypropylene bottles, tightly sealed and refrigerated. After field sampling, samples will be transported to a water quality analysis laboratory for approximately four hours or less. In the lab, samples will be kept in the dark refrigerator at around 4°C between 12 to 24 hours to ensure the samples are not exposed to any light or heat to prevent degradation of Chl-a. During the analysis, the Chl-a water samples will first be filtered using paper fibre (Whatman GF/C), then extracted from the water samples using 90% acetone, followed by centrifugation for 10 to 20 minutes at about 4000 rpm in the centrifugal machine. The spectrophotometer will finally be used to measure the Chl-a content in the samples.

Turbidity is a measure of light scattering caused by suspended particles in natural waters (Robert et al., 2017; Sakuno et al., 2018). It is a measure of water clarity, and high turbidity levels generally indicate poor water quality. Turbidity is usually reported in formazin turbidity units (FTU) units or the equivalent nephelometric turbidity units (NTU). In this study, the analysis of the seschi depth (**Error! Reference source not found.**) is used to measure clarity b ecause in situ observations for this variable are easy to collect. A Secchi disk (20/30cm radius) will be used to measure turbidity at each sampling location in the dam. The disk will be lowered

slowly into the water using an attached rope on the shady side of the boat until it is no longer visible. Where the rope enters the water, it will be marked to measure (in metres) how far the disk had to be lowered into the dam until it was no longer visible. This process will be repeated twice to ensure the accuracy of the measurements. The GPS location of the sampling points will be recorded.

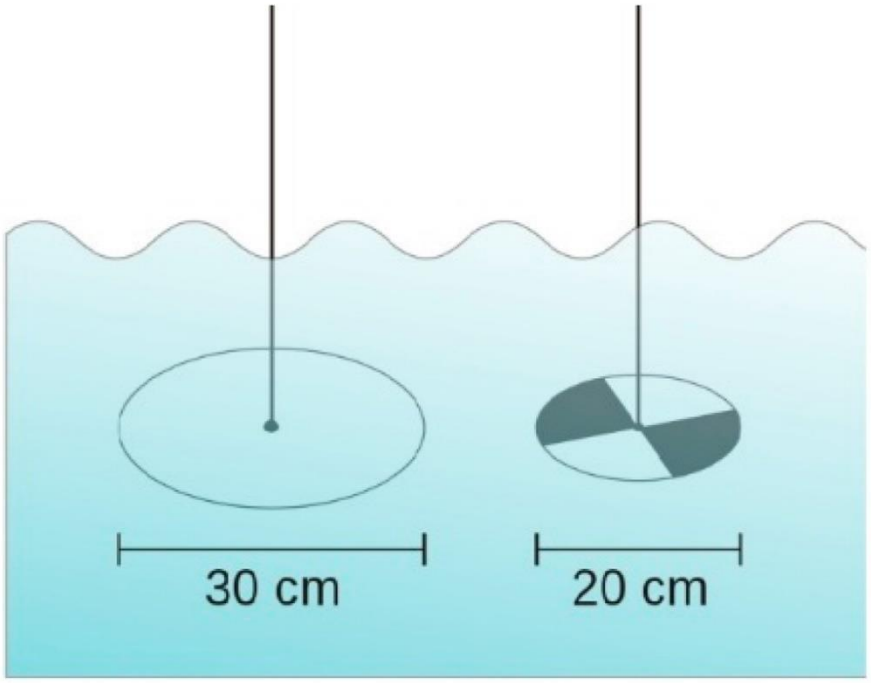

Figure 3: Two different kinds of Seschi disks with different diameters

ii. Remotely sensed data

The UAV carrying the MicaSense will be flown over the reservoirs around noon, regarding the sun angle (between 30° and 60° to minimize sun-glint effects and specular reflections). *N* ground control points will be distributed evenly in the flight area, and x,y, and z coordinates will be surveyed with a GPS with sub-metric precision. The flight mission will be planned as a simple grid with a distance between flight lines of 20-45 m. and a flight height of 120 m; the drone's speed has to be set. Depending on the sampling frequency of the in-situ device, *n* measurements will be recorded within 15 minutes of the sensor overpass. Validation protocol (Lee, 2006) commonly advises to average in-situ measurements that fall within a temporal window of 1 to 4 h of the sensor overpass. No atmospheric correction will be applied to the

UAV imagery, as the effect of the thin atmosphere layer between the sensor and the water surface is neglected.

The image's geo-referencing, radiometric processing and mosaicking will be performed with the Pix4D software (Pix4D, Lausanne, Sw.). Raw multispectral images will be corrected to ground absolute reflectance using the irradiance measures taken along with each snapshot by the MicaSense sensor onboard the UAV and spectrally rescaled against a calibration panel with values around 70 % of diffuse reflectance in the visible-infrared spectrum. The image information extraction will be done at different sampling sizes corresponding to the median of all the pixel values using QGIS 2.18.15.

3.1.2 Water level and quantity

The summer season often sees a decline in water levels in agricultural canals and reservoirs. The study will analyse surface water dynamics over the wet and dry periods of the selected catchment reservoirs. Ground measurements will be used to validate remotely sensed observations.

i. Ground truth observations

In-situ observations will be obtained with the levelling technique (**Error! Reference source not found.**). Water level data from ground stations should fulfil certain requirements to use them for validating altimetry measurements from remotely sensed. Firstly, the ground stations must be very short from the sensor ground track. This helps in minimizing measurement errors due to location. These errors may be due to the backwater effect, tidal waves, or both. Secondly, the date and time measurements of the gauge and altimetry data must match to make comparisons. Poles of the same height will be located along the area of interest (e.g. along the canal) to have stable in-situ reference points. These poles' horizontal and vertical coordinates are measured on multiple days (one measurement every week during the dry period) with a GNSS rover station Trimble RTK GNSS R8s. The offset between the metal pole and the closest water surface point will be measured with the levelling instrument Leica Sprinter 50 Digital Level. Levelling generally ensures sub-mm accuracy in height difference determination. Measurements will be done during calm days to minimise errors from waves and ripples.

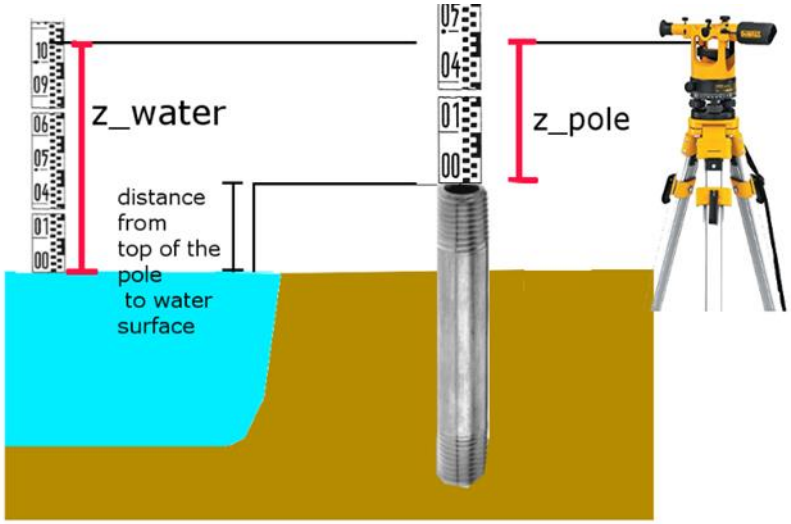

Figure 4: Levelling system for in-situ ground-truth observations. Vertical absolute poles coordinates were measured with an RTK GNSS system.

ii. Remotely sensed data

Regarding water level measurements, the Global Navigation Satellite System (GNSS) is the most plausible practical candidate for measuring the water level in reservoirs. LIDAR and GNSS receivers can be mounted on the UAVs (**Error! Reference source not found.**). Several e xperimental flights will be conducted over the reservoirs between 1200 and 1400 SAST at approximately 90, 100 and 120m height. In all the flights, the wind speed must be minimal, approximately less than 1.5m/s. The time series of the measured altitude of the UAV and the estimated heights will be recorded.

The vertical distance of the receiver antenna from the sea surface (h) can be separately determined together with the GNSS antenna height (H_a) to obtain the water surface height (H_S) (**Error! Reference source not found.**). With knowledge of the relative position between a U AV and a GNSS satellite, and the assumption of a flat, non-tilted reflection surface, the difference in the geometric ranges between the direct and reflected signal paths, and delay, can be calculated.

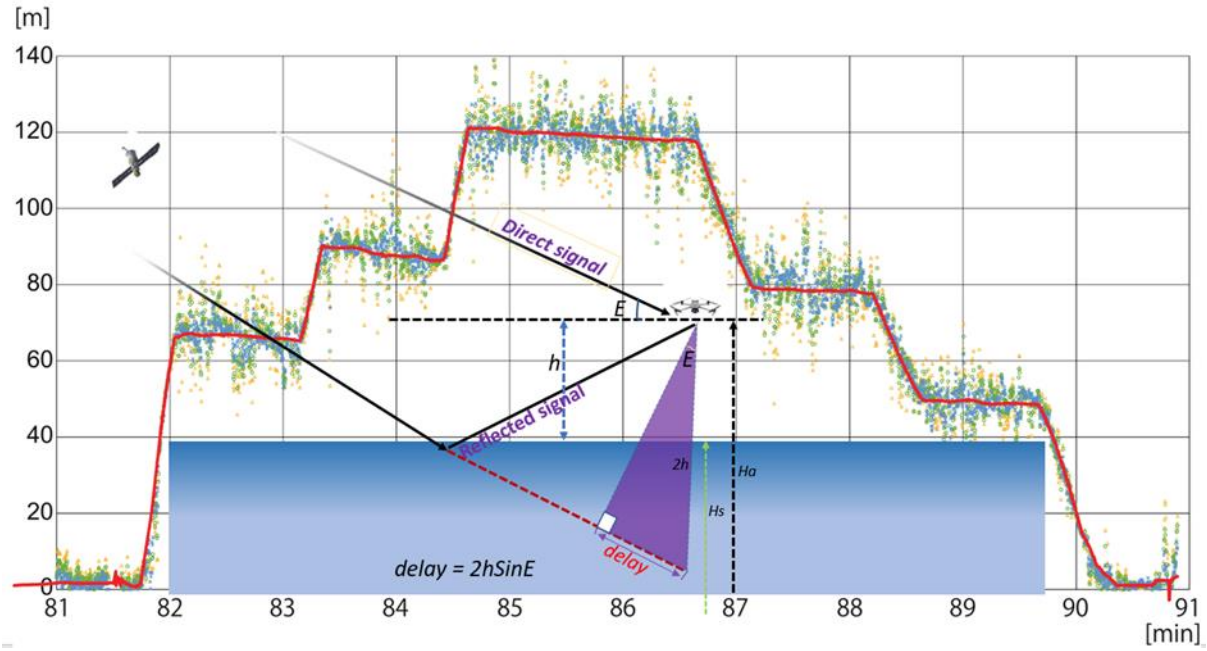

Figure 5: Schematic diagram showing UAV flight to retrieve water surface elevation observations

3.1.3 Flood mapping in agricultural canals

Presently, around one million hectares of South Africa are under irrigation, accounting for approximately 62% of total national water use (Adetoro et al., 2020). Large volumes of water are transported through thousands of kilometres of irrigation canal systems across the country, all of which experience a level of flooding. It is estimated that a minimum average of 20% to 30% of the water supplied to the irrigation sector is lost due to leakages out of conveyance structures, evaporation, spillage and flooding, among others. Flooding and leaks contribute to the highest loss.

i. Ground sampling

Floods in irrigation canals are caused by intensive precipitation over long periods, causing the river to overflow its banks, and ultimately inundating the neighbouring areas (Karaoui et al., 2019). This process is slow and can last for several days. Flood inundation mapping is similar to water body mapping while facing some challenges, such as the short response time and cloud cover. In this study, the rainfall data near the canals will be used to track the rainfall patterns in the catchment. The location of the irrigation database in vector format will be obtained from

relevant departments in the target locations. The database will contain polygons representing canals as determined during extensive field surveys done by the relevant departments in the target locations. During fieldwork, ground data will be collected, including measurements of the flood extent, surveys, interviews and mobile photographs. A well-distributed network of ground control points (GCP) for the flooded areas will be collected using a hand-held Trimble Juno 3D (Differential GPS) with sub-metre accuracy.

ii. Remotely sensed data

The remotely sensed data will be collected by flying the DJI M-300 drone during the flooding days. Designing and executing a good image acquisition plan for flood mapping is the most important part of any drone mapping project. The ultimate accuracy of the flood depth depends upon the quality of the images. Drone Deploy, an app with cross-device support, a web interface, and the DJI GS Pro app, will be used for flight path generation and execution. The images are acquired along a flight path, like a scanner, where the software finds the most efficient path up and down a specific area of interest (AOI) that coincides with the points collected during the field campaign. The overlap is set to 75% for both sideways and forward directions, with a flight altitude of less than 100 m. The images will be radiometrically corrected and geo-referenced.

3.2 Experimental design and drone imagery

Reservoirs and irrigation canals in the selected catchments, with diverse characteristics and extents, will be chosen to evaluate the performance of the proposed methods and techniques. The first step is to delineate the extent of these reservoirs.

The DJI Matrice 300 (DJI M-300) drone, mounted with a MicaSense Altum camera and a GPS, will be used to capture aerial images over the reservoirs and agricultural canals in the selected catchments. The MicaSense Altum camera is a multispectral and thermal-imaging sensor that integrates five narrow spectral bands (blue, green, red, red-edge, and near-infrared) (**Error! R eference source not found.**). The spectral range spans the visible region and a portion of the near-infrared (NIR) region, from 400 nm to 1000 nm. These bands have a sensor resolution of 2064 × 1544 at 120 m (3.2 megapixels per multispectral band) and a ground sample distance (GSD) of 5.2 cm per pixel at 120 m height suggesting the optimum flight altitude above the

water surface to receive high-resolution images. The camera also has a 48° × 37° Field Of View (FOV) with an 8 mm focal length.

Table 2: The wavelengths and bandwidths for the MicaSense sensor

Band	Center (nm)	Band Width (nm)	Range (nm)
Blue	475	32	443 – 507
Green	560	27	533 – 587
Red	668	16	652 – 684
Red Edge	717	12	705 – 729
Near Infrared (NIR)	842	57	785 – 899

3.3 Methodology

Error! Reference source not found.6 is a graphical representation of the processes and p rocedures used to explore the importance of drones in enhancing food and water security. The procedure is informed by the need to monitor water quality and quantity of water reservoirs in light of climate change to maintain water and food security. The challenge requires innovative, efficient and cost-effective technologies to improve agricultural water management and enable smallholder farmers to improve productivity under water-limited conditions without increasing pressure on already strained water resources or constructing other dams.

This project is designed to estimate (i) water quality, (ii) monitor temporal and spatial changes in water quantity and (iii) flood mapping using UAV imagery. Furthermore, types of spatial, temporal and spectral resolution sensors for monitoring the quality and quantity of surface water resources will be covered in detail.

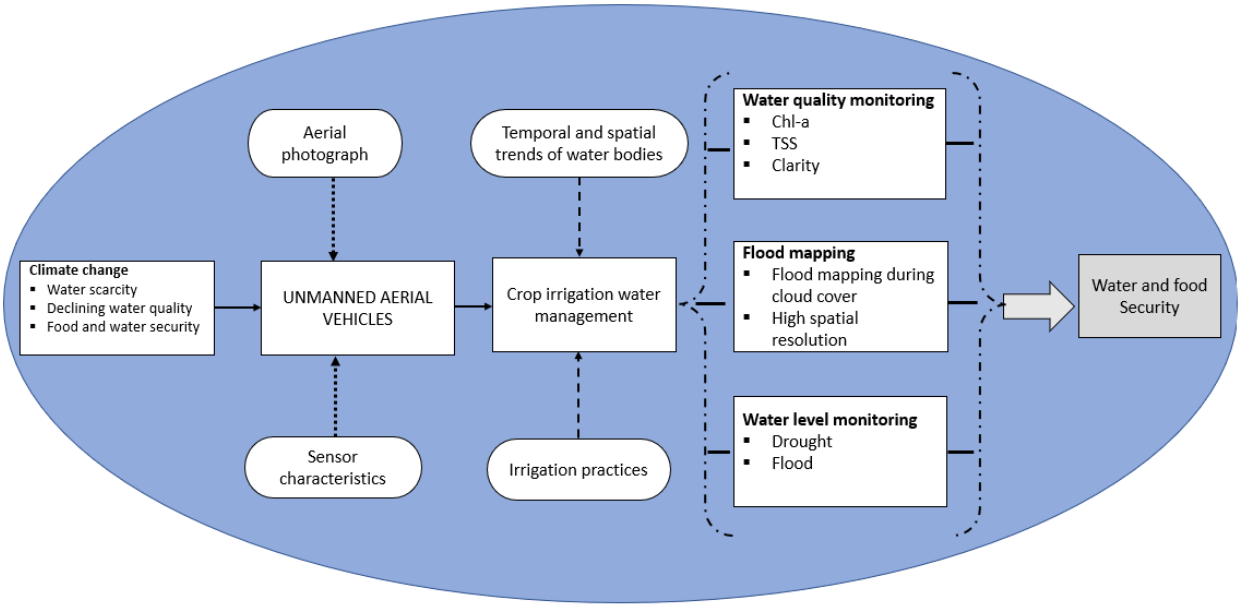

Figure 6: Methodological framework to explore the importance of UAVs in surface water management for food security

3.3.1 Estimating water quality using UAVs

The first step is to create a water-only image by applying unsupervised or supervised classification as described in the flooding or water level sections. Because water has spectral characteristics distinct from terrestrial features, water pixels will be grouped into one or a few distinct classes that could be easily identified. This can be achieved by further classifying the image based on the spectral profile and location of pixels. The classes can include open water and shallow water (where bottom sediments and/or macrophytes affected spectral response). These areas tend to have high spatial variability compared to open-water portions of the rivers. Based on this analysis, affected pixels can be removed.

Next, the spectral-radiometric data from the “open water” images will be extracted from the areas around the sampling locations to develop relationships with in-situ water quality data. For this purpose, we will use each sample's imagery and GPS locations to delineate a polygon in a spectrally-radiometrically similar area (identified visually using different band combinations stretched to a range of water-only pixels) around each sample location. The number of pixels will depend on the pixel size. For example, 30 m imagery can have a minimum of 200 pixels in narrow portions of the rivers or areas with high heterogeneity and

up to 1700 pixels in wider, more homogeneous areas. The signature editor in ERDAS Imagine will be used to extract spectral and radiometric data from the polygons. Mean band values from the polygons will be imported into Microsoft Excel, ratios and differences for band combinations will be calculated, and data from the ground-based measurements and samples will be linked to the appropriate imagery samples.

A suitable water quality retrieval algorithm is the key step to link the water leaving reflectance to the water quality variables in remote sensing of water quality (Lee, 2006; Salama et al., 2012). Especially in inland reservoirs, where not only a high concentration of nutrients and dissolved organic substances can occur but also a mixing of Chl_a, TSS and blue-green algae. In synergy with in situ measurements, remote sensing of water is an important tool for monitoring the trophic status of inland waters. A major interest in using remote sensing data in aquatic environments is to ascertain the spatial and temporal variation of the water composition and investigate the origin and displacement of specific suspended or dissolved substances. However, not all water quality parameters can be estimated using remote sensing techniques (Ritchie et al., 2003; Sibanda et al., 2021). TSS, algae, DOM, oils, aquatic vascular plants, and thermal releases change the energy spectra of reflected solar and/or emitting thermal radiation from surface waters which can be measured using remote sensing techniques and are known as optically active components. Most chemicals and pathogens do not directly affect or change surface water's spectral or thermal properties, so they can only be inferred indirectly from measurements of other water quality parameters affected by these chemicals (Ritchie et al., 2003).

To develop models to predict water quality variables from the imagery products, the project will perform empirical relationships between spectral properties and water quality parameters. The general forms of these empirical equations are:

$$Y = a + bX \qquad \text{or} \qquad Y = ab^X$$

where Y is the remote sensing measurement (i.e., radiance, reflectance, energy), X is the water quality parameter of interest (i.e., suspended sediment, Chl-a), and a and b are empirically derived factors.

i. Chl-a

Chl-a is the main pigment in all phytoplankton, with varying amounts per taxonomic group (Gitelson, 1992). It is widely used as a proxy in determining phytoplankton concentration in water bodies. Estimating Chl-a concentrations from remotely sensed imagery requires the development of algorithms with maximum sensitivity for the concentration of this pigment and minimum sensitivity to the concentration of other components present in the water (Gitelson, 1992; Ritchie et al., 2003). Thus, estimating this Chl-a for inland waters using remote sensing is challenging since the optical properties of these types of water are significantly influenced by mineral particles, sediments, and organisms associated with phytoplankton (Gitelson, 1992).

Simple models of water colour (optical spectral reflectance) for a range of values of Chl-a concentrations will be derived based on the work of Gitelson (1992) and Gower et al. (1999). These models were developed based on the observation that water reflectance spectra for lower Chl-a concentration (<30 mgm^{-3}) peak at 685 nm and the peak in the wavelength range 700–710 nm for higher Chl-a concentrations. For developing the empirical models, linear fits will be applied, expressing the relationships between radiance/reflectance at different wavelengths of the micasense sensor in every match-up point and their corresponding "in situ" water parameter data as a linear function of the format:

$$Chl_a(mgm^{-3}) = a + b \times SBC$$

where *a* and *b* are the model parameters (intercept and slope, respectively), and *SBC* is the tested Spectral Band Combination. *SBC*s can either be an index, a ratio or an algorithm. Some of these combinations (of two and three bands) are those proposed by different authors and will be adapted to MicaSense spectral bands in this project.

The results from the parametric models can be compared to band ratios of near-infrared (NIR)/red (R) and NIR/blue (B) as well as other vegetation indices such as the green normalized difference vegetation index (GNDVI) and normalised difference vegetation index (NDVI) will be computed. GNDVI is based on two-band combinations of the red-edge region of the spectrum and is very sensitive to the change in chlorophyll content, which is related to the nitrogen content.

i. Total suspended solids

Total suspended solids (TSS) is the mass concentration (mg/L) of particles small enough (< a few mm) to remain suspended in the water column by natural levels of turbulence and large enough to be collected on a filter with a specified pore size (Caballero et al., 2014; Chen et al., 2015). Under normal conditions, turbulence keeps such particles suspended on timescales of hours to days (or even longer), but they eventually settle by gravity and are deposited to reservoir bottoms. Before they settle, they reduce the clarity of the water. Suspended sediments are the most common pollutant in weight and volume in the surface waters of freshwater systems. Suspended sediments increase the radiance emergent from surface waters in the visible and near-infrared proportion of the electromagnetic spectrum (Ritchie et al., 2003).

Error! Reference source not found.7 shows a relationship between suspended sediments and r adiance or reflectance from spectral wave bands or combinations of wave bands on remote sensing sensors. The wavelengths between 700 and 800 nm are most useful for determining suspended sediments in surface water.

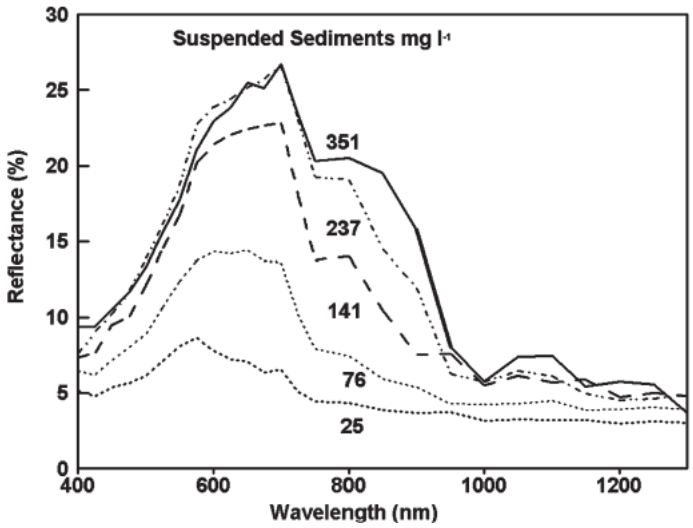

Figure 7: The relationship between reflectance and wavelength as affected by the concentration of suspended sediments (Adapted from Ritchie et al. (2003))

Empirical relationships (algorithms) between the concentration of suspended sediments and radiance or reflectance for a specific date and site will be developed in this study using the scattering peak at 700nm. The Iterative Stepwise Elimination Partial Least Squares Regression (ISE-PLS) will be used to estimate TSS. To improve the performance of the partial least squares (PLS) regression model, the optimum wavelengths with good predictive ability are selected for

model calibration. The wavelengths elimination process depends on the importance of the predictors (C_i), described as follows:

$$C_i = \frac{|\beta_i| S_i}{\sum_{i=1}^{I} |\beta_i| S_i}$$

where $\beta_i$is the regression coefficient and S_i is the standard deviation of the predictor, both corresponding to the predictor variable of the waveband *i*.

Initially, all available wavebands of the hyperspectral sensor (400–900 nm) will be used to develop the PLS regression model. Then variables are ranked from most contributed to least contributed according to the predictor C_i; in other words, the predictor$C_i$represents the weight of each variable. The least contributed variable is eliminated, and the PLS model is recalibrated with the remaining predictor variables (Forina et al., 2004). The model-building procedure is repeated, and in each cycle, the predictor variable with the minimum importance (i.e., the less informative wavelength) is eliminated until the final variable is eliminated. To determine the optimum number of wavelengths to include in the final model, LOO cross-validation is conducted after each calibration. The final model with the maximum predictive ability is calibrated by the minimum value of root mean squared error (RMSE) (D'Archivio et al., 2014).

ii. Seschi disc transparency (SDT)

This project will adopt regression analysis of micasense bands and nearly contemporaneous ground observations. To develop models to predict SDT variables from the imagery products, nonlinear power and step-wise multiple regression model will be developed and used.

3 shows the models that will be adopted in this study. This empirical approach requires carefully timed and spatially distributed field measurements. Typically, two or three consecutive scenes along a single track will be combined (resulting in a single regression model). The resulting regression model will then be applied to the image data for all reservoirs in each scene, either on a whole-reservoir level (using the spectral signatures extracted previously) or an individual-pixel level.

Regression statistics will be calculated for the relationship between the natural log of SDT and remotely sensed single bands, band ratios and multiple bands, successively increasing the time window between sensor overpass and ground observation from same-day ground observations. Previous studies have used models to address the curvilinear behaviour of the relationship between ground and remotely sensed observations.

Table 3: Retrieval models of total suspended solids (TSS) using regression models

Model	References
$\log(C_{SDT}) = a + b * \log R(710)$	Kallio et al. (2001)
$C_{SDT} = a * (b * R(645))$	Miller and McKee (2004)
$C_{SDT} = a\,(R(660))^{b}$	Isidro et al. (2018)
$C_{SDT} = \frac{a * R(825)}{1 - \left(\frac{R(825)}{c}\right)} - d$	Caballero et al. (2014)
$\log(C_{SDT}) = \frac{-b \pm \sqrt{b^2 - 4a(c - \frac{logR(865)}{logR(655)}}}{2a}$	Wang et al. (2018)
$C_{SDT} = a * (R(645))^2 + b * R(645)$	Ondrusek et al. (2012)
$Neural\ network$	Chen et al. (2015)

NOTE: *a*, *b* and *c* are regression model coefficients where independent variables are the observed spectral radiance values from the respective bands.

iii. Other parameters, such as nutrients and DO

However, nutrients (i.e., total nitrogen and phosphorus) concentrations, dissolved oxygen levels, and microorganisms/pathogens are not optically active. Given that nutrients are significant factors in the initiation, propagation, and growth of Chl-a, it is imperative to estimate their concentrations. Ratio indices are often constructed using the scattering peak at the red edge (700 nm), the reflectance troughs caused by chlorophyll absorption at 670 nm, and pigment absorption at 592 or 620 nm can be used to predict total nitrogen and total phosphorus.

Deep learning architectures, including recurrent and convolutional neural networks, appear particularly attractive due to their great success in many recent studies, outperforming many other methods in a variety of remote sensing applications that will be adopted in this study (Ma et al., 2019).

3.3.2 Flood mapping

UAVs provide an affordable and flexible solution for gathering information critical for effective flood risk assessment and response to a flood event in small- to medium-scale areas. The ability to quickly deploy UAVs allows access to real-time aerial information about detecting and mapping flooding extents or leaks along irrigation canals and dams. Monitoring the evolution of a flood event provides first responders with information to better prioritize resources in dangerous situations.

shows the spectral water indices used to map leaks and crop fields' flooded areas. These spectral indices successfully delineate clear waters, but this project's challenge is to delineate floods in crop fields. The challenge is mixed pixels, affecting the spectral profile, thus underestimating the flooded area. However, the high spectral, spatial and temporal resolution of sensors onboard UAVs will estimate the flooded area of crop fields with better accuracy.

When it comes to stream flooding, drones are essential for accurate and detailed streamflow measurement, which include (i) optimization of workflows to enable extraction of terrestrial and subsurface topographies through accurate image registration using automatic or direct geo-referencing techniques; (ii) the determination of water levels through the image- and turbulence-derived metrics; and (iii) the derivation of flow velocities through appropriate techniques based on the characteristics of flow, duration of observation, seeding density.

High spatial resolution (< 1m) drone images of river width, water depth and flow velocity can be used as a surrogate to represent discharge variations and be used in flood monitoring. The drone images will be geo-referenced and projected into the Universal Transverse Mercator coordinate system (UTM Zone 36). The average river width (W_e) at a river segment upstream of the station will be measured from space. Because of the spectral characteristics and high spatial resolution of the drone images, it is feasible to determine the water surface area (A_t) (m^2) with relatively high precision using visual interpretation and delineating the area defined by the edge of the water surface adjacent to the river channel. The area of the dry channel (A_s) (m^2) can then be determined, and the difference between (A_t) and (A_t) is the water surface area in the specified river segment (A_w) (m^2). The length of the central line of the river channel (L) (m) is measured from the drone images. The equation below will be used to calculate (W_e)

$$W_e = \frac{A_w}{L} = \frac{A_t - A_s}{L}$$

Different regression methods can then be used to model the relationship between an observed and measured discharge.

3.3.3 Water levels and quantity

The optical sensor onboard the drone will serve the purpose of measuring surface water. Increasing the spatial resolution of sensors has been a key goal of remote sensing research,

hence introducing high spatial resolution multispectral sensors onboard drones. These can provide images with spatial resolutions at a meter or even sub-meter level. Water boundaries cannot be easily distinguished over a mixed pixel; however, water levels in water bodies can be detected successfully using multispectral sensors at higher resolution.

The principle of extracting surface water from optical images is the obviously lower reflectance of water in infrared channels compared to that of other land cover types. Based on this principle, several algorithms have been developed to extract water levels using multispectral sensors. An easy and effective way to extract water is to use water indices, calculated from two or more bands, to identify the differences between water and non-water areas. The only challenge is to select optimum band combinations and the optimum threshold, especially in polluted or vegetated water bodies.

Several water indices will be tried and tested in this study.

4 shows some of the indices that will be tested for delineating water surfaces in the selected catchments. However, some studies have successfully used vegetation indices such as NDVI to delineate water surfaces. Therefore, vegetation indices will not be spared in this project. Spectral indices will be derived from the MicaSense Altum sensor to map the spatial and temporal changes of water bodies in the selected catchments.

Thresholding is one of the most critical issues in using water indices to extract water bodies. Based on the reflectance characteristics of water, spectral indices values for water are usually greater than 0. Therefore, a threshold of 0 is often applied to extract water from index images (Bangira et al., 2019; Xu, 2006). However, adjustment of the threshold value usually achieves better extraction results. This is especially tricky when thresholding either a time series of images that cover the same water body or a single image that covers a group of water bodies because automation would be impossible if manual adjustments on the threshold value for each image were required (Bangira et al., 2019; Fisher et al., 2016). An automatic histogram-based thresholding algorithm, Otsu's method (Otsu, 1979), selects threshold values that maximize the between-class variances of the histogram and will be used.

Table 4: Popularly used spectral indices for delineating water bodies

Index	Equation	Source
Normalized difference water index (NDWI)	$\frac{(GREEN - NIR)}{(GREEN + NIR)}$	McFeeters (1996)
modified NDWI (mNDWI)	$\frac{(GREEN - SWIR)}{(GREEN + SWIR)}$	Xu (2006)
Automated water extraction index (AWEI)	$4 \times (\text{GREEN} - \text{SWIR}) - (0.25 \times \text{NIR} + 2.75 \times \text{SWIR})$	Feyisa et al. (2014)
Water index (WI)	$x + a(GREEN) + y(RED) - b\ (NIR) - c \times SWIR_1 - d(SWIR_2)$ x, y, b, c *and* d *are values to be determined by the us*	Fisher et al. (2016)

The threshold value t separating these classes is determined by a set of equations as outlined in (Otsu, 1979) as follows:

$$\delta^2 = P_{nw} . (M_{nw} - M)^2 + P_w . (M_w - M)^2, \quad (1)$$

$$M = P_{nw} . M_{nw} + P_w . M_w \quad (2)$$

$$P_{nw} + P_w = 1 \quad (3)$$

$$t^* = \underset{a \le T \ge b}{Arg\ Max} \{P_{nw} . (M_{nw} - M)^2 + P_w . (M_w - M)^2\} \quad (4)$$

where δ is the inter-class variance of the non-water class and the water class; P_{nw} and P_w are the probabilities of one pixel belonging to non-water and water, respectively; M_w and M_{nw} are the mean values of the non-water and water classes; and M is the mean value of the feature image.

The supervised machine learning algorithms such as random forest (RF), support vector machine (SVM), constant optimisation parameter SVM (*c*-SVM, decision trees (DTs) and *k*-NN, which are established in remote sensing, will be used to classify the image. These algorithms are simple, flexible and computationally efficient (Bangira et al., 2019).

The exponential, power and polynomial models will be used to fit the relationship between a reservoir's in situ measurements and satellite observations. These models are used to fit the relationship to find the optimal relationship between the in situ-observed water levels and micasense measurements. **Error! Reference source not found.**8 summarizes the m ethodological framework when it comes to the use of drone imagery for estimating the water level of a reservoir.

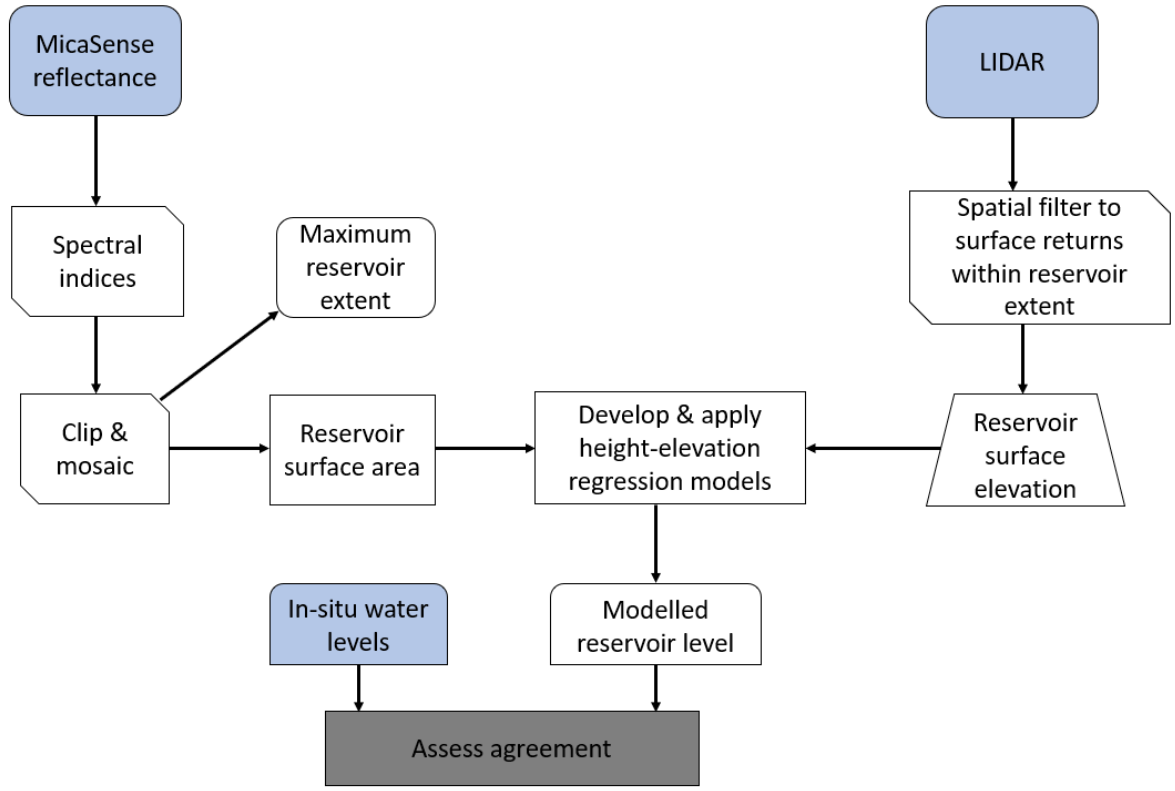

Figure 8: Multispectral image processing and measurement of water levels

3.4 Model validation

A 3:2 sample split ratio will be employed for classifier and accuracy assessment, as suggested in many studies. The number of test samples needed for accuracy testing will be based on the multinomial distribution for a confidence interval of 95% for the accuracy assessment (Congalton and Green, 2019). Testing samples per class will be determined based on the percent coverage calculated from an initial unsupervised classification, as suggested by (Ballanti et al., 2016). The non-water classes will be combined (reclassified) into one class, namely non-water, to assess the binary thresholding experiments. The same training (input) and testing (validation) datasets will be used for all the classification experiments to ensure that differences in accuracy could be attributed to the nature of the class allocation processes.

A producer's accuracy (PA), user's accuracy (UA), overall accuracy (OA), and the kappa coefficient (K) will be generated for each classification experiment. OA is easily interpreted as it represents the percentage of classified pixels in the image that have been correctly labelled.

At the same time, K can be used to assess statistical differences between classifications (Ballanti et al., 2016). The statistical significance of the accuracy differences among experiments will be evaluated using non-parametric statistical tests, such as McNemar's and Friedman's, as implemented in the Statistical Package for Social Sciences (SPSS). Differences will be considered statistically significant at $p < 0.05$.

Statistical indicators such as root-mean-square error (RMSE), absolute relative error (ARE), bias, and mean absolute error (MAE) between the measured and predicted values will be used to evaluate the remote sensing inversion models used.

3.4.1 Datasets to be developed include

i. Flood maps
ii. Water quality maps
iii. The concentration of water parameters
iv. Spatial and temporal patterns of water bodies in the selected catchments
v. Flood depths estimates
vi. Water levels and quantity

3.5 Developing datasets

3.5.1 Hardware and software environment

The multispectral MicaSense Altum with DLS 2 sensor and DJI Matrice 300 drone are available. The drone has a maximum payload capacity and maximum take-off weight of 2.7 kg and 9 kg, respectively. The Altum integrates five high-resolution narrow bands with a radiometric thermal camera, producing advanced multispectral and thermal imagery in a single flight. The multispectral bands have a sensor resolution of 2064 × 1544 at 120 m (400 ft) and a ground sample distance of 5.2 cm per pixel. The thermal infrared sensor has a resolution of 160 × 120 at 120 m (400 ft) and a ground sample distance of 81cm per pixel at 120m. The DLS

2 is the light sensor accompanied by the camera. DLS 2 is an innovative technology used for irradiance and sun angle measurements. It provides more accurate and reliable data, substantially improves radiometric accuracy, and reduces post-processing time. **Error! R eference source not found.**5 gives the details of the camera's multispectral and thermal infrared lenses.

Table 5: Multispectral bands and band widths (nm) of Altum sensor

Band	Spectral Bands	Centre (nm)	Band Width (nm)	Resolution: 2064 × 1544 at 120m (MP)
1	Blue	475	20	3.2
2	Green	560	20	3.2
3	Red	668	10	3.2
4	Red Edge	717	10	3.2
5	Near-Infrared	840	40	3.2
6	Long Wave Infrared (LWIR)	Thermal Infrared	8-14um	×120 at 120m

4 REFERENCES

Adetoro, A.A., Abraham, S., Paraskevopoulos, A.L., Owusu-Sekyere, E., Jordaan, H., Orimoloye, I.R. (2020) Alleviating water shortages by decreasing water footprint in sugarcane production: The impacts of different soil mulching and irrigation systems in South Africa. Groundwater for Sustainable Development 11, 100464.

Ballanti, L., Blesius, L., Hines, E., Kruse, B. (2016) Tree Species Classification Using Hyperspectral Imagery: A Comparison of Two Classifiers. Remote Sensing 8, 445.

Bangira, T., Alfieri, S.M., Menenti, M., Van Niekerk, A. (2019) Comparing thresholding with machine learning classifiers for mapping complex water. Remote Sensing 11, 1351.

Caballero, I., Morris, E.P., Ruiz, J., Navarro, G. (2014) Assessment of suspended solids in the Guadalquivir estuary using new DEIMOS-1 medium spatial resolution imagery. Remote Sensing of Environment 146, 148-158.

Chen, J., Quan, W., Cui, T., Song, Q. (2015) Estimation of total suspended matter concentration from MODIS data using a neural network model in the China eastern coastal zone. Estuarine, Coastal and Shelf Science 155, 104-113.

Congalton, R.G., Green, K. (2019) Assessing the accuracy of remotely sensed data: principles and practices. CRC press.

D'Archivio, A.A., Maggi, M.A., Ruggieri, F. (2014) Modelling of UPLC behaviour of acylcarnitines by quantitative structure-retention relationships. J Pharm Biomed Anal 96, 224-230.

Feyisa, G.L., Meilby, H., Fensholt, R., Proud, S.R. (2014) Automated Water Extraction Index: A new technique for surface water mapping using Landsat imagery. Remote Sensing of Environment 140, 23-35.

Fisher, A., Flood, N., Danaher, T. (2016) Comparing Landsat water index methods for automated water classification in eastern Australia. Remote Sensing of Environment 175, 167-182.

Forina, M., Lanteri, S., Oliveros, M.C., Millan, C.P. (2004) Selection of useful predictors in multivariate calibration. Analytical and Bioanalytical Chemistry 380, 397-418.

Gholizadeh, M.H., Melesse, A.M., Reddi, L. (2016) A Comprehensive Review on Water Quality Parameters Estimation Using Remote Sensing Techniques. Sensors 16, 1298.

Gitelson, A. (1992) The peak near 700 nm on radiance spectra of algae and water: relationships of its magnitude and position with chlorophyll concentration. International Journal of Remote Sensing 13, 3367-3373.

Gower, J.F.R., Doerffer, R., Borstad, G.A. (1999) Interpretation of the 685nm peak in water-leaving radiance spectra in terms of fluorescence, absorption and scattering, and its observation by MERIS. International Journal of Remote Sensing 20, 1771-1786.

Isidro, C.M., McIntyre, N., Lechner, A.M., Callow, I. (2018) Quantifying suspended solids in small rivers using satellite data. Science of The Total Environment 634, 1554-1562.

Kallio, K., Kutser, T., Hannonen, T., Koponen, S., Pulliainen, J., Vepsäläinen, J., Pyhälahti, T. (2001) Retrieval of water quality from airborne imaging spectrometry of various lake types in different seasons. Science of The Total Environment 268, 59-77.

Kapalanga, T.S., Hoko, Z., Gumindoga, W., Chikwiramakomo, L. (2021) Remote-sensing-based algorithms for water quality monitoring in Olushandja Dam, north-central Namibia. Water Supply 21, 1878-1894.

Karaoui, I., Arioua, A., Boudhar, A., Hssaisoune, M., El Mouatassime, S., Ouhamchich, K.A., Elhamdouni, D., Idrissi, A.E., Nouaim, W. (2019) Evaluating the potential of Sentinel-2 satellite images for water quality characterization of artificial reservoirs: The Bin El Ouidane Reservoir case study (Morocco). Meteorology Hydrology and Water Management-Research and Operational Applications 7, 31-39.

Kibena, J., Nhapi, I., Gumindoga, W. (2014) Assessing the relationship between water quality parameters and changes in landuse patterns in the Upper Manyame River, Zimbabwe. Physics and Chemistry of the Earth 67-69, 153-163.

Kim, G., Baek, I., Stocker, M.D., Smith, J.E., Van Tassell, A.L., Qin, J., Chan, D.E., Pachepsky, Y., Kim, M.S. (2020) Hyperspectral Imaging from a Multipurpose Floating Platform to Estimate Chlorophyll-a Concentrations in Irrigation Pond Water. Remote Sensing 12, 2070.

Kirk, J.T. (1994) Light and photosynthesis in aquatic ecosystems. Cambridge university press.

Kundzewicz, Z.W., Krysanova, V., Benestad, R., Hov, Ø., Piniewski, M., Otto, I.M. (2018) Uncertainty in climate change impacts on water resources. Environmental Science & Policy 79, 1-8.

Lee, Z.-P. (2006) Remote Sensing of Inherent Optical Properties: Fundamentals, Tests of Algorithms, and Applications. International Ocean Colour Coordinating Group (IOCCG).

Ma, L., Liu, Y., Zhang, X., Ye, Y., Yin, G., Johnson, B.A. (2019) Deep learning in remote sensing applications: A meta-analysis and review. ISPRS Journal of Photogrammetry and Remote Sensing 152, 166-177.

McFeeters, S.K. (1996) The use of the Normalized Difference Water Index (NDWI) in the delineation of open water features. International Journal of Remote Sensing 17, 1425-1432.

Miller, R.L., McKee, B.A. (2004) Using MODIS Terra 250 m imagery to map concentrations of total suspended matter in coastal waters. Remote Sensing of Environment 93, 259-266.

Modiegi, M., Rampedi, I.T., Tesfamichael, S.G. (2020) Comparison of multi-source satellite data for quantifying water quality parameters in a mining environment. Journal of Hydrology 591, 125322.

Ondrusek, M., Stengel, E., Kinkade, C.S., Vogel, R.L., Keegstra, P., Hunter, C., Kim, C. (2012) The development of a new optical total suspended matter algorithm for the Chesapeake Bay. Remote Sensing of Environment 119, 243-254.

Otsu, N. (1979) A Threshold Selection Method from Gray-Level Histograms. IEEE Transactions on Systems, Man, and Cybernetics 9, 62-66.

Ritchie, J.C., Zimba, P.V., Everitt, J.H. (2003) Remote sensing techniques to assess water quality. Photogrammetric Engineering & Remote Sensing 69, 695-704.

Robert, E., Kergoat, L., Soumaguel, N., Merlet, S., Martinez, J.M., Diawara, M., Grippa, M. (2017) Analysis of Suspended Particulate Matter and Its Drivers in Sahelian Ponds and Lakes by Remote Sensing (Landsat and MODIS): Gourma Region, Mali. Remote Sensing 9.

Sakuno, Y., Yajima, H., Yoshioka, Y., Sugahara, S., Abd Elbasit, M.A.M., Adam, E., Chirima, J.G. (2018) Evaluation of Unified Algorithms for Remote Sensing of Chlorophyll-a and Turbidity in Lake Shinji and Lake Nakaumi of Japan and the Vaal Dam Reservoir of South Africa under Eutrophic and Ultra-Turbid Conditions. Water 10, 618.

Salama, M.S., Radwan, M., van der Velde, R. (2012) A hydro-optical model for deriving water quality variables from satellite images (HydroSat): A case study of the Nile River demonstrating the future Sentinel-2 capabilities. Physics and Chemistry of the Earth 50-52, 224-232.

Sibanda, M., Mutanga, O., Chimonyo, V.G., Clulow, A.D., Shoko, C., Mazvimavi, D., Dube, T., Mabhaudhi, T. (2021) Application of drone technologies in surface water resources monitoring and assessment: A systematic review of progress, challenges, and opportunities in the global south. Drones 5, 84.

Tebbs, E.J., Avery, S.T., Chadwick, M.A. (2020) Satellite remote sensing reveals impacts from dam-associated hydrological changes on chlorophyll-a in the world's largest desert lake. River Research and Applications 36, 211-222.

Van der Zel, D. (1975) Umgeni River catchment analysis. Water SA 1, 70-75.

Wang, C., Li, W., Chen, S., Li, D., Wang, D., Liu, J. (2018) The spatial and temporal variation of total suspended solid concentration in Pearl River Estuary during 1987–2015 based on remote sensing. Science of The Total Environment 618, 1125-1138.

Xu, H. (2006) Modification of normalised difference water index (NDWI) to enhance open water features in remotely sensed imagery. International Journal of Remote Sensing 27, 3025-3033.

Zaman, M., Shahid, S.A., Heng, L., (2018) Irrigation Water Quality, in: Zaman, M., Shahid, S.A., Heng, L. (Eds.), Guideline for Salinity Assessment, Mitigation and Adaptation Using Nuclear and Related Techniques. Springer International Publishing, Cham, pp. 113-131.

Zhou, H., Gumbo, V. (2021) Rural-urban comparison of manufacturing SMMEs performance in KwaZulu Natal province, South Africa. African Journal of Development Studies 11, 7-31.

Annex: INSTRUMENTS and SOFTWARE

LIDAR sensor

LIDAR sensor specifications

Drone Platform DJI Matrice 300

Supplier: TBA

Name of system: DJI ZENMUSE L1 LIDAR SYSTEM or RIEGL VQ-840-G

Amount: TBC

Description: The Zenmuse L1 integrates a Livox Lidar module, a high-accuracy IMU, and a camera with a 1-inch CMOS on a 3-axis stabilized gimbal. The L1 has high efficiency, covering 2 km^2 in a single flight with a high vertical accuracy of 5cm and a horizontal accuracy of 10cm. It has a point rate of 240000 pts/s and a detection range of 450 m.

Hyperspectral sensors

Sensitivity studies spanning a range of diverse aquatic water bodies recommend hyperspectral sensors bandwidths of 5 nm.

Hyperspectral sensor specifications

Drone Platform DJI Matrice 300

Supplier: TBA

Name of system: Gaiasky-mini Hyperspectral Imaging Camera

Amount: TBC

Spectral Range 400 - 1000 nm
Spectral Resolution 2.1 nm
Spectral Channels 281
Spectral Pixels 561
Spatial Channels 900
Max Frame Rate 249 fps
Signal-to-Noise Ratio (peak) 368 (2x bin)-520 (4x bin)
Bit Depth 12 Focal Length (nm) 17
FOV (deg),
IFIV (mrad) 17.6, 0.88
Weight 0.6 kg
Dimensions (cm) 10.0 x 12.5 x 5.3

SOFTWARE

The software used throughout the research may include the following: ArcGIS 10.8; Pix4Dfields; QGIS Desktop 3.22; ENVI, ERDAS; Li-DARMill of Phoenix LiDAR Systems, R-statistical package, python.